Polymer Testing 151 (2025) 108960

Contents lists available at ScienceDirect

Polymer Testing

journal homepage: www.elsevier.com/locate/polytest

Non-destructive assessment of strain and mechanical fatigue in neat and glass fibre-reinforced epoxy via NIR spectroscopy

Daniel Esse [a,*], Gabriel Sick [a], Frank Henning [b], Bodo Fiedler [c], Wilfried V. Liebig [a]

[a] Karlsruhe Institute of Technology, Institute for Applied Materials - Materials Science and Engineering, Engelbert-Arnold-Straße 4, Karlsruhe, 76131, Germany
[b] Karlsruhe Institute of Technology, Institute for Vehicle Systems Engineering, Rintheimer Querallee 2, Karlsruhe, 76131, Germany
[c] Hamburg University of Technology, Institute of Polymers and Composites, Denickestraße 15, Hamburg, 21073, Germany

ARTICLE INFO

Keywords:
Damage assessment
Peak shift
Composite
DGEBA
Infrared spectroscopy

ABSTRACT

In this study, changes in the near-infrared (NIR) spectrum in neat epoxy and glass fibre-reinforced plastic under tensile stress and cyclic fatigue loading are investigated. Specimens were fabricated using resin transfer moulding. During mechanical testing, NIR spectra were collected at regular intervals, enabling monitoring of characteristic absorption bands. Results demonstrate that both material systems show measurable and reproducible shifts in the wavenumber of the absorbed light in specific NIR bands as a function of applied mechanical load. These shifts closely track the progression of damage accumulation, particularly in the context of mechanical fatigue. Overall, the findings underscore the potential of NIR spectroscopy as a powerful, non-destructive, in-situ monitoring tool for assessing the integrity and damage evolution of fibre-reinforced plastic under mechanical stress. This approach provides valuable insights for the development of advanced structural damage monitoring systems and contributes to improving the safety and reliability of composite materials in engineering applications.

1. Introduction and motivation

Infrared (IR) spectroscopy is a well-established and reliable measurement method for characterising the chemical properties of materials, such as polymers and resins. The chemical composition of the materials can be determined and, e.g., the morphological, orientation or deformation phenomena of the molecules can be examined [1–3]. Mechanical stresses or environmental conditions on polymer materials lead to temporary and permanent changes at molecular level. In order to enhance the utility of spectroscopic techniques, it is essential to comprehend and quantify the various effects on the spectra.

Infrared light is absorbed by a molecule under certain conditions. The initial premise is the Bohr frequency condition $\delta E = h\nu$, which states that the energy $h\nu$, with the frequency ν and the Planck constant h, of infrared light, must be equivalent to a discrete energy difference δE between two vibrational energy levels of a molecular bond [4].

A transition from the ground vibrational state to the first excited state is referred to as fundamental. A combination band is defined as a band in which transitions occur for at least two vibrations at one wavenumber. If the energy of the light is so high that one vibrational mode is increased by at least two energy levels, the band is categorised as an overtone. [5]. The first overtone is thereby at a wavenumber that is almost double that for the corresponding fundamental band.

In order to evaluate changes in material properties that are not related to chemical alterations, the peak shift is utilised as a means of measuring these variations. The maxima of specific bands were thereby determined to undergo a change in wavenumber under specific conditions, including mechanical elongation, temperature, and moisture [6–8]. This approach was explored in 1964 by Reynolds and Sternstein, who published a report on the peak shift of the $-OH$ and $-NH$ stretching bands across various materials [6]. Further attempts were made to calculate the internal stress distribution with the curve shape and the peak shift [9]. Later, Salmén and Bergström examined the peak shift in cellulose in dry and moist conditions [10]. Their findings revealed that, while the peak shift remained consistent for the strain under both conditions, it showed differences when the material was subjected to stress.

A molecule comprising N atoms has 3N - 6 distinct vibrational modes. If the molecule has a linear structure, it can exhibit 3N - 5 vibrational mode. Consequently, a diatomic molecule exhibits one vibrational mode, which occurs in the form of a stretching vibration [5]. To elucidate a possible mechanism for the peak shift, the phenomenon of quasielastic deformation, it is most straightforward to consider a

* Corresponding author.
E-mail address: daniel.esse@kit.edu (D. Esse).

https://doi.org/10.1016/j.polymertesting.2025.108960
Received 22 July 2025; Received in revised form 14 August 2025; Accepted 22 August 2025
Available online 30 August 2025

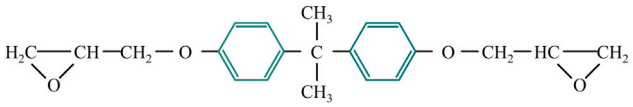

(a) DGEBA

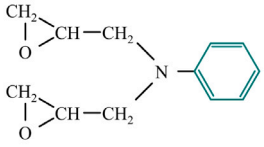

(b) N-(Oxiranylmethyl)-N-phenyl-oxiranmethanamine

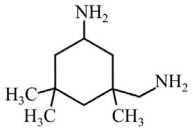

(c) Isophorondiamine

Fig. 1. Molecular structures of the resin and hardener components.

vibrating molecular bond as a two-mass oscillator or even a harmonic oscillator. The frequency ν for a harmonic oscillator is defined by Eq. (1), in which m represents the mass and k denotes the force constant of the connecting spring. Given that the mass is constant, a reduction in k is the only factor capable of causing a decrease in frequency [11].

$$\nu = \frac{1}{2\pi}\sqrt{\frac{\mathbf{k}}{m}} \tag{1}$$

The relationship between the internuclear distance and the force constant was elucidated by Badger, who reported that the bond stiffness of a diatomic molecule is inversely proportional to the bond length [12]. His initial formulation was subsequently subjected to numerous refinements [13]. Reynolds and Sternstein provided an explanation for the weakening of a bond with increasing external pressure and the resulting peak shift, which they attributed to the strengthening of an adjacent hydrogen bond [6]. A similar explanation for the peak shift in cellulose was proposed by Salmén and Bergström for an increase in strain [10]. In the case of more complex molecules, the wavenumber of the absorbed light is dependent on the angle between two bonds [11]. If the molecule is subjected to deformation, an angular change will result in a change in frequency. In the case of a nonlinear triatomic molecule, the symmetric stretching vibration mode was found to be the most stress-sensitive. Furthermore, conformational changes, such as internal rotations coupled with the aforementioned mechanism and defects, such as chain ends or chemical defects, will result in a shift in the wavenumber of the absorbed light [11].

During the course of this study, tensile tests are carried out using glass-fibre-reinforced epoxy and the neat matrix material. The load is applied stepwise, allowing near infrared spectra to be measured at regular intervals during the test. Moreover, reinforced specimens are subjected to a cyclic mechanical load, with intermittent measurements of NIR spectra and crack density. The spectra are analysed to identify peak shift, correlated with the strain or stiffness degradation and compared between different specimen types.

2. Material and methods

2.1. Material system and manufacturing

The tests are carried out on continuous fibre-reinforced epoxy resin and the matrix material itself, consisting of the Resoltech 1500 resin based on diglycidyl ether of bisphenol A (DGEBA) and N-(Oxiranylmethyl)-N-phenyl-oxiranmethanamine combined with the Resoltech 1504 hardener based on 3-aminomethyl-3,5,5-trimethylcyclohexylamine (isophorondiamine). The molecular structures are shown in Fig. 1. The aromatic rings are marked thereby in green, as they were focused on in the NIR evaluation.

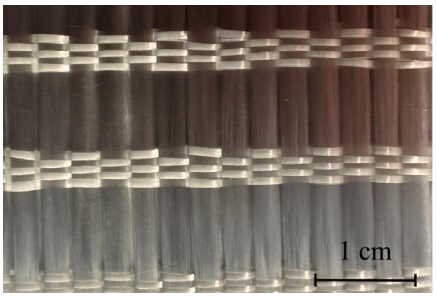

Fig. 2. Unidirectional E-glass fibre fabrics.

For unidirectional (UD) reinforced specimens GFRP $[0]_{2s}$, four layers of unidirectional E-glass fibre fabrics shown in Fig. 2, provided by HaLarit Composites, with an areal weight of 416 g/m^2 are used and manufactured with an orientation of 0° relative to the loading direction. The fibre fabrics consist of 408 g/m^2 weft yarn and 8 g/m^2 warp yarn, both of which are produced from the same material. Biaxially reinforced specimens are manufactured with eight layers of the same weft yarn arranged in a $[+45/-45]_{2s}$ lay-up.

The material is manufactured using resin transfer moulding (RTM). Once the fibre fabrics are placed in the moulds, which are 1.25 mm thick for the UD GFRP $[0]_{2s}$ specimens and 2.5 mm thick for the biaxial GFRP $[+45/-45]_{2s}$ specimens, the resin is injected. This is done by applying a pressure of 3 bar on the inlet side and a vacuum on the opposite side within a vacuum chamber, with the aim of removing the air and excess resin. The final fibre volume content is 50 %. Post-curing is carried out according to the manufacturer's instructions to achieve a T_g of 141 ° C. The samples are cut according to DIN EN ISO 527 from the panels by waterjet cutting.

2.2. Stepwise tensile testing with NIR spectroscopy

Tensile tests are performed force-controlled on a Zwick Roell 100 kN universal testing machine for the neat epoxy and GFRP specimens. An additional 20 kN load cell is used for neat epoxy specimens. The strain is measured using a digital image correlation (DIC) system, GOM Correlate, provided by Zeiss. The DIC measurement is conducted by applying five reference point markers on either side of the specimens. Stress is applied in incremental steps of 3600 N for the GFRP $[0]_{2s}$ specimens and 300 N (12 MPa) for the neat epoxy. For the GFRP $[+45/-45]_{2s}$ specimens, a load of 1500 N (24 MPa) is applied in the first four steps and 750 N in the fifth. Owing to increasing plastic deformation, the manner in which the load is applied is modified to strain controlled, with an increase of 0.6% for each step. The results of the stepwise tensile tests show the average of a set of three specimens.

NIR measurements are conducted using the Bruker FT-NIR Process Spectrometer Matrix F, with a recorded wavenumber range of 12,000 cm^{-1} to 4,000 cm^{-1}. The NIR light was directed towards the specimen and subsequently collected using an optical fibre cable coupled with a reflectance probe. Owing to the material's high transparency, spectral quality was improved by positioning a reflective surface behind the sample. Consequently, measurements were performed in transflection mode. The spectra are recorded with a resolution of 2 cm^{-1}, with 20 measurements taken around the middle of the specimen for each load step. The measurement positions are taken on a 2 × 10 raster with 3 mm distances between each point, which is automated with the help of stepper motors.

2.3. Interrupted fatigue testing with NIR spectroscopy

Fatigue tests are conducted under stress-controlled conditions, a load ratio of 0.1 and at a frequency of 1 Hz to avoid heating of the

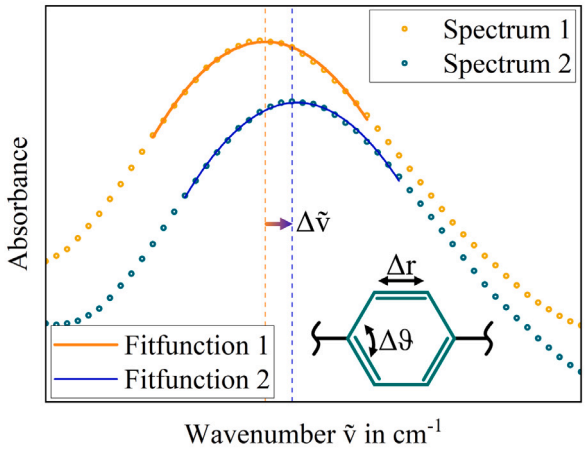

Fig. 3. Systematic visualisation of the peakshift owing to a change in bond angle $\Delta\vartheta$ or bond length Δr calculated by the horizontal shift of a fitfunction.

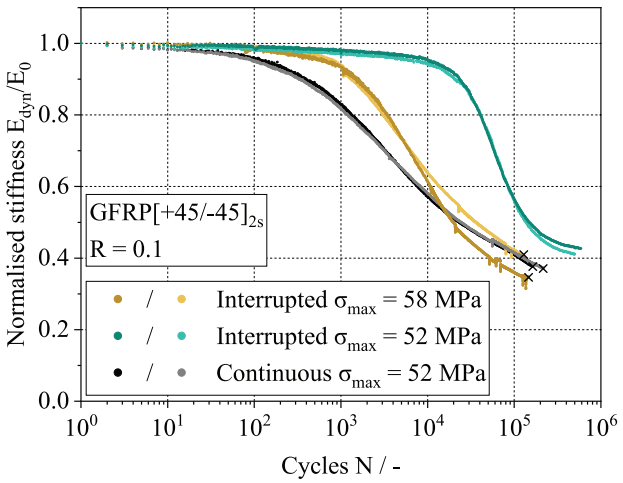

Fig. 4. Normalised stiffness degradation of GFRP $[+45/-45]_{2s}$ specimens under cyclic loading for two maximum stresses, with comparison of interrupted and continuously conducted tests.

specimens owing to internal friction. The maximum load capacity is established at 52 MPa or 58 MPa, corresponding to 0.36 and 0.40 of the ultimate testing strength. The force is quantified using a 1220AJ load cell from Interface and the strain is determined with an A50-5 o clip-on extensometer from Sandner, with a testing length of 50 mm. Both measurements are taken at a frequency of 200 Hz.

For the purpose of NIR measurements, the experimental procedure is interrupted and the sample is unloaded. The measurements are conducted in a manner consistent with the tensile tests. The NIR spectra of the specimens at 0.4 UTS are measured additionally two months after breaking in order to evaluate decreasing residual stresses.

For light microscopy, the tests are unmounted and examined at an Axiovert 200 MAT from Zeiss. In order to evaluate the impact of these interruptions, a series of tests are conducted without interruptions. For every parameter, two specimens are tested. For the examination with a scanning electron microscope (SEM) the Leo Gemini 1530 from Zeiss is used.

2.4. Processing of the measurement

The recorded data from the extensometer and load cell are evaluated for specimen stiffness by fitting the individual strain and stress cycles to a sinusoidal curve and dividing the amplitudes of stress and strain. It is expected that the changes in wavenumber for certain bands will be smaller than the resolution of the spectroscope. To resolve this issue, the wavenumber of the individual bands is determined by fitting each band with a fifth-degree polynomial, as shown systematically in Fig. 3 for a peak shift induced by a change in bond angle $\Delta\vartheta$ or bond length Δr. The maximum of the polynomial is determined as the wavenumber of the band. The peak shift is quantified as the change in wavenumber of the 20 measurements at each load stage relative to the initial 20 measurements of the unloaded specimen. The standard deviation is computed by performing pairwise comparisons between each measurement of the current stage and all measurements of the initial stage, followed by calculating the standard deviation of the resulting differences.

3. Results

The mechanical behaviour of the normalised stiffness $\frac{E_{dyn}}{E_0}$ of GFRP $[+45/-45]_{2s}$ during the cyclic fatigue tests over the logarithmic number of cycles is shown in Fig. 4. Specimens that are assessed using identical testing procedures are distinguished by different colour shades. The lower load tests are not run to failure owing to the extended duration of the experiment. At the beginning of the test, the stiffness remains close to the initial stiffness. Subsequent to the initial plateau, the curves demonstrate a gradual, steady decrease in stiffness as the number of cycles increases. Especially for lower load, the degradation gradually levels off as the curve progresses. The interrupted tests for both load levels exhibit a similar shape, but the plateau for the test conducted at 58 MPa is shorter, leading to a horizontal shift of about one decade compared to the test at 52 MPa. The initial stiffness for the tests at 0.36 UTS is around 13.6 GPa. In the continuous tests, stiffness declines earlier but with a gentler slope after the plateau, resulting in a comparable number of cycles until failure, ranging from $1.3 \cdot 10^5$ to $2.2 \cdot 10^5$.

Fig. 5 demonstrates the range of damage types that could be identified during the lifetime at the higher load of 0.4 UTS, while Fig. 6 shows the damages just before or after breakage. Off-axis matrix cracks in the outer layers, which predominantly originate from the cutting edge of the specimen, are the first damage pattern that appears. The cracks exhibit a length of multiple centimetres already at 100 cycles. These cracks grow in number and size during fatigue loading in all layers. As illustrated in Fig. 5(a), cracks can be observed externally to the focal plane, indicating their presence in the underlying layers. The subsequent damage type to be observed is the formation of multiple cracks along the warp yarns on the specimen's surface, over an off-axis matrix crack, located beneath the warp yarn, as shown in Fig. 5(b) for a specimen exposed to 10^4 cycles. The warp yarns are interlaced in plain weaves, as shown in Fig. 2. Consequently, the off-axis matrix cracks below are in one roving. Furthermore, areal damage to the underlying layer can be identified in the brighter area out of the focal plane. Fig. 5(c) depicts a SEM image of the aforementioned damage for a specimen which is already failed. The image displays the impregnated warp yarn in the top right corner and the off-axis matrix crack in the weft roving originating from the lower left corner. Along the warp yarn, numerous small cracks and partial matrix detachment can be seen, while in the weft yarn along the crack, debonded fibres are evident. At the point of intersection between the weft yarn and the warp yarn, a broken and debonded fibre from the warp yarn is visible. As the stiffness degradation slowed down at approximately $6 \cdot 10^4$ cycles, delamination occurred at the cutting edges. As shown in Fig. 5(d) at higher magnification in the light microscope, the separation of the individual layers from each other is discernible, with an opening of the size of the glass fibres themselves. Furthermore, delamination with an off-axis matrix crack connection to the surface of the specimen could also be detected, as demonstrated in Fig. 5(e) for a polished edge

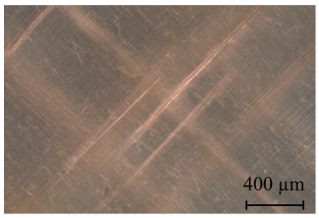

(a) Off-axis matrix cracks in the first ply after 10^3 load cycles.

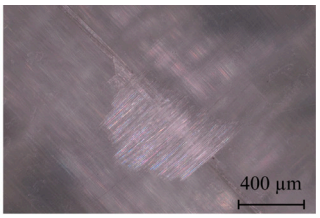

(b) Multiple matrix cracks along the sewing yarn after 10^4 load cycles and areal damage between first and second ply.

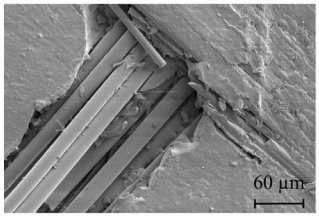

(c) Off-axis matrix cracks under the sewing yarn and cracks along the fibres of the sewing yarn.

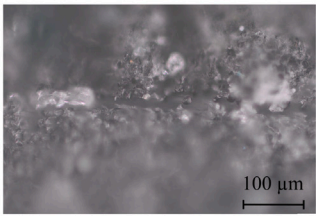

(d) Delamination at the cutting edge after $6 \cdot 10^4$ load cycles.

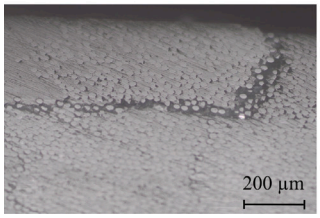

(e) Delamination at the cutting edge after $9 \cdot 10^4$ load cycles.

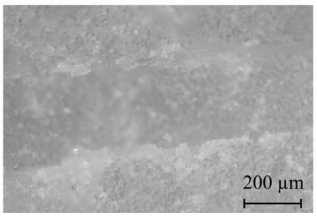

(f) Shift of the individual plies to each other after $1.4 \cdot 10^5$ load cycles.

Fig. 5. Light microscope, SEM and camera images of damages in GFRP $[+45/-45]_{2s}$ specimens exposed to a variety of mechanical load cycles at 0.4 UTS.

of a specimen at $9 \cdot 10^4$ cycles. As the level of damage increases, a concomitant decrease in both the material's cross-sectional area and its transparency is observable. A shift of the individual layers to each other is observable in Fig. 5(f). The outer plies depicted in the image are aligned at the focus level, while the layer positioned centrally is more deeply etched.

The image in Fig. 6(a) was taken at the section exhibiting the lowest transparency levels and consequently the most damage, where the specimen subsequently failed and only a few cycles before the specimen failed. The uppermost laminate layer exhibits a crack width that exceeded 100 µm in certain areas, accompanied by a crack extending to the surface. Additionally, glass fibres are observed to be displaced from the cutting edge of the test specimen along the entire section. The specimen's failure is demonstrated in Fig. 6(b) and Fig. 6(c), which depict areas of delamination and breakage of the rovings that are located further away from the edges of the specimen. The subsequent two figures present SEM images of the fractured section. In Fig. 6(d) for a broken fibre roving and in Fig. 6(e) for an area of delamination. Both images show substantial areas of debonding and some evidence of plastic deformation in the epoxy. Examples include the leftmost section in the image showing delamination, and the middle-left fibres in Fig. 6(d).

A comparison of the NIR absorption spectra of the neat epoxy and GFRP $[+45/-45]_{2s}$ is illustrated in Fig. 7. The two spectra show the same maxima, albeit with slight variations in intensity. As assigned in Table 1 the majority of the bands arise from OH and CH modes, with one NH band originating from the epoxy curing agent.

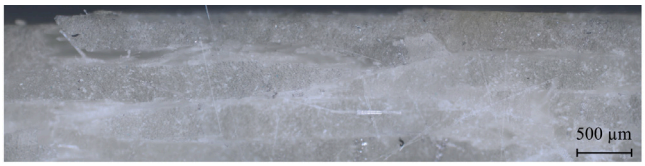

(a) Strong delamination between multiple plies and pushed out fibres at area with the highest damage accumulation $1.6 \cdot 10^5$ load cycles.

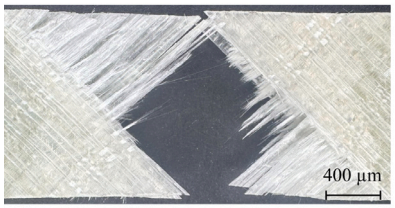

(b) Overview of broken specimen, showing areas of delamination and broken rovings.

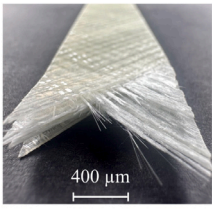

(c) Broken specimen showing areas of delamination and broken rovings.

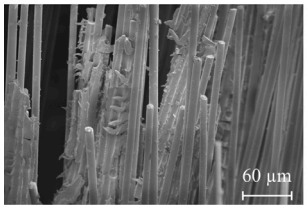

(d) SEM image of broken rovings after specimen failure.

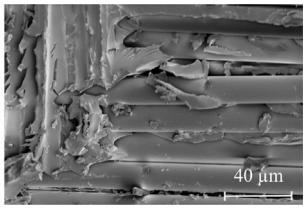

(e) SEM image of delaminated area after specimen failure

Fig. 6. Light microscope, SEM and camera images of damages in GFRP $[+45/-45]_{2s}$ after or just before breakage owing to mechanical load cycles at 0.4 UTS.

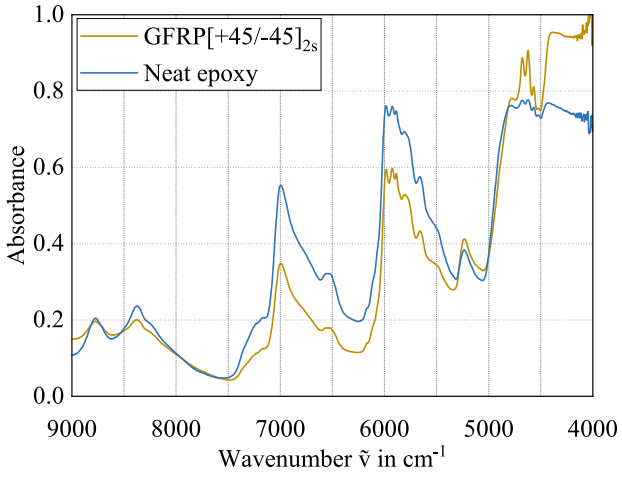

Fig. 7. NIR absorption spectrum of DGEBA based glass fibres reinforced epoxy in comparison to the neat epoxy.

The peak shift measured in the stepwise tensile test is shown on the left of Fig. 8, while the results of the cyclic mechanical fatigue test are shown in Fig. 9. Both peak shifts are calculated from CH combination bands, with the band at $\tilde{\nu} = 4390\ \mathrm{cm}^{-1}$ arising from the aromatic -CH band that exists only in the epoxy chains.

Fig. 8(b) shows the peak shift for the band at around $\tilde{\nu} = 4566\ \mathrm{cm}^{-1}$. A linear trend of approximately $-0.15\ \mathrm{cm}^{-1}\,\%^{-1}$ can be seen for all specimens. As the GFRP $[+45/-45]_{2s}$ specimens undergo significant deformation, the measurement covers a greater range of strain with the maximum mean value just above $-1\ \mathrm{cm}^{-1}\,\%^{-1}$ at 6.2% strain. With further strain, the peak shift is declining. For the same band in the

Table 1
Vibration mode of molecules at specific wavenumber for Resoltech 1500/1504 epoxy.

Wavenumber in cm^{-1}	Vibrational mode	Ref.
4350	Combination band of aromatic $-CH$	[14]
4520	Combination of $-CH$ stretching, $-CH_2$ deformation and $-CH-CH_2-O$ fringe group	[15–19]
4567	Aromatic combination of $C=C$ stretching and $-CH$ stretching	[20]
4621	Aromatic combination of $C=C$ stretching and $-CH$ stretching	[16,17,21]
4676	Aromatic combination of $C=C$ stretching and $-CH$ stretching	[16–18]
4782	Combination band of $-OH$	[16,17]
5236	Combination of asymmetric $-OH$ stretching and H_20 bending vibration	[5,15,21]
5656	Combination of $-CH$ and $-CH_2$ overtones	[22]
5804	Combination of $-CH$ and $-CH_2$	[14]
5885	First overtones of the fundamental $-CH_2$ and $-CH$ stretching vibration	[14,22]
5924	Combination of $-CH_2$ and $-CH$	[23]
5983	First overtones of $-CH$ and $-CH_2$ stretching vibrations	[16,17,21,22]
6541	Overtone of primary amine $-NH_2$ stretching and secondary amine $-NH$ stretching	[6,15,17,19,21]
6996	First overtone of $-OH$ stretching vibration	[5,17–19,21]
8376	Second overtone of a $-CH_3$ stretching vibration	[20]

fatigue tests, the peak shift is shown in Fig. 9(b) with the same colour shades as in the stiffness degradation, no significant peak shift can be observed for this band, instead the scattering increases after 10^3 cycles. The measurements taken two months after the breakage are marked with solid circles instead of hollow ones and show no significant shift as well.

The peak shift of the band, which is initially measured at $\tilde{\nu} = 4390\ cm^{-1}$, is shown in Fig. 8(a) and Fig. 9(a). No peak shift can be measured in the linear elastic region for the tensile test. A negative peak shift is determined for the GFRP $[+45/-45]_{2s}$, increasing quickly before slowing down gradually to a final value of approximately -60 cm^{-1} prior to breaking. Initially, the standard deviation increases, before reaching lower values again towards the end.

Similar behaviour can be observed in the fatigue tests shown in Fig. 9(a), with a peak shift of a similar size and a reduction in standard deviation prior to breaking, particularly at the higher load level of 0.4 UTS. The decrease in band wavenumber at the lower load level shifts by about one decade to a higher number of cycles. Two months after breaking, the measurements are at the same wavenumber as prior to breaking, with a standard deviation. A more detailed analysis of the GFRP $[+45/-45]_{2s}$ band reveals that it exhibits rather discrete than continuous behaviour between the two wavenumbers of the spectrum at around $\tilde{\nu} = 4390\ cm^{-1}$ and 4320 cm^{-1}, as shown in Fig. 10. The density of the calculated peak shift is illustrated for five steps in the stepwise tensile test (Fig. 10(a)) and for the cyclic mechanical tests (Fig. 10(b)). The different stages are visualised using a colour gradient ranging from yellow for the virgin specimen to blue for the specimen just before it breaks. Along with the load, a decrease in density at 0 cm^{-1} and a continuous increase around -70 cm^{-1} can be observed.

4. Discussion

The observed stiffness degradation in GFRP $[+45/-45]_{2s}$ specimens under cyclic loading exhibits distinct patterns, influenced by both applied stress levels and testing methodology. As reported by Demers, the anticipated number of load cycles until breakage is 10^5 at 0.4 UTS [24]. Consequently, the tests conducted in this study have yielded outcomes that are commensurate with the initial expectations, or have demonstrated a marginally higher number of load cycles. At 0.36 UTS (52 MPa), stiffness degradation progresses gradually after an initial plateau. For 0.4 UTS (58 MPa), the plateau phase is shorter, accelerating the reduction in stiffness by approximately one decade in the number of cycles. Consequently, the pattern is the same as that seen in the shift of the aromatic -CH peak at the former wavenumber of $\tilde{\nu} = 4390\ cm^{-1}$ and the shift between the two load levels can also be recognised in the publication by Drvoderic [25]. The key mechanisms driving stiffness loss include:

- Matrix cracks: Off-axis cracks originating predominantly from specimen cutting edges propagate through weft yarns.
- Fibre-matrix debonding: SEM images reveal interfacial failure along cracks.
- Delamination: Layer separation initiates predominantly at cutting edges and progresses inward, exacerbated by cyclic shear stresses in the biaxial GFRP $[+45/-45]_{2s}$ layup.
- Fibre breaking: The sample breaks as soon as the residual strength is exceeded by the cyclic load, resulting in rupture of the rovings.

Furthermore, cracks in the matrix surrounding the warp yarns expose these rovings on the surface, likely originating from the stretching of the initially undulated weft yarn. The same progression for the stiffness reduction for angle-plies was measured by Wharmby and Ellyin [26] and Drvoderic [25]. It was asserted that the termination of the plateau in stiffness, or the commencement of stiffness reduction, corresponds with the onset of visual cracks. Moreover, it was observed likewise that both cracks and delamination were initiated at the free edges [26]. The initial decline in stiffness can be attributed primarily to crack growth. Wharmby et al. state that the cracks reach a saturation state, and the damage mode changes to delamination. For the latter damage growth, the rate of stiffness reduction is considerably less than the first damage mode [27]. The interruptions in testing introduce stiffness recovery artifacts at the cycle counts where crack growth is the dominant degradation mechanism, as evidenced by shorter degradation plateaus compared to continuous tests. This suggests that viscoelastic relaxation during measurement pauses partially restores molecular-scale interactions or slows down crack growth, although macroscopic damage remains irreversible. Similar conclusions were reached by Movahedi-Rad et al. who reported that "fatigue stiffness was partially restored after each loading interruption due to the recovery of the viscoelastic polymeric matrix. This repeated material stiffening at the beginning of each loading block delayed crack growth" [28].

The similarity of the absorption spectra of GFRP and neat epoxy shows that epoxy has the highest absorptivity by considerable degrees. The difference in absorption intensity may be owing to a different baseline, potentially caused by light scattering from the fibres or a chemical influence from the glass fibre sizing agents.

A comparable shift in the peak at wavenumber $\tilde{\nu} = 4566\ cm^{-1}$ is observed in all specimen types during the stepwise tensile tests. It is demonstrated that an increase in stress, and consequently strain, results in a rising negative shift. A negative peak shift with rising strain on a load-bearing molecular bond has already been observed [10], and can be explained by the Badger-Bauer rule [12,13]. The decreasing shift above 6 % strain may be due to a redistribution of the load from the matrix to the fibres. As the fatigue testing proceeds, an increase in the

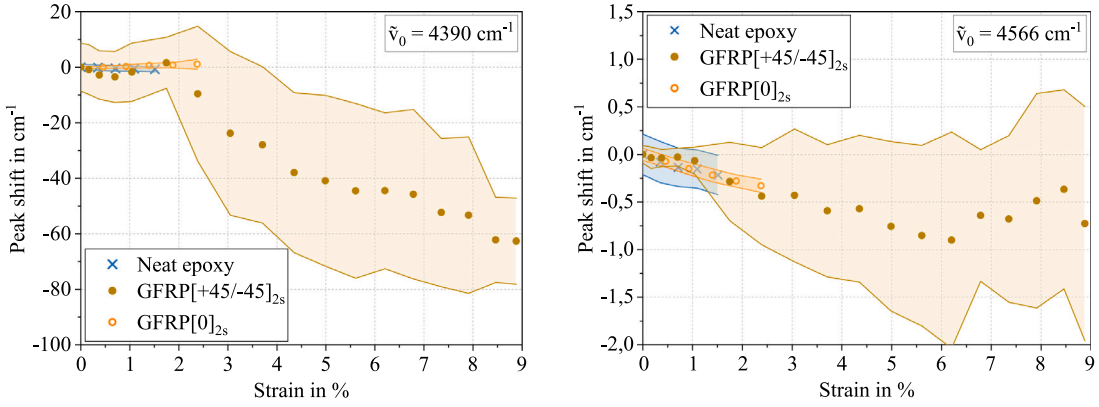

(a) Peak shift of the aromatic combination band at $\tilde{\nu}$ = 4390 cm^{-1} (b) Peak shift of the aromatic combination band at $\tilde{\nu}$ = 4566 cm^{-1}

Fig. 8. Peak shift over the mechanical strain during the stepwise tensile test.

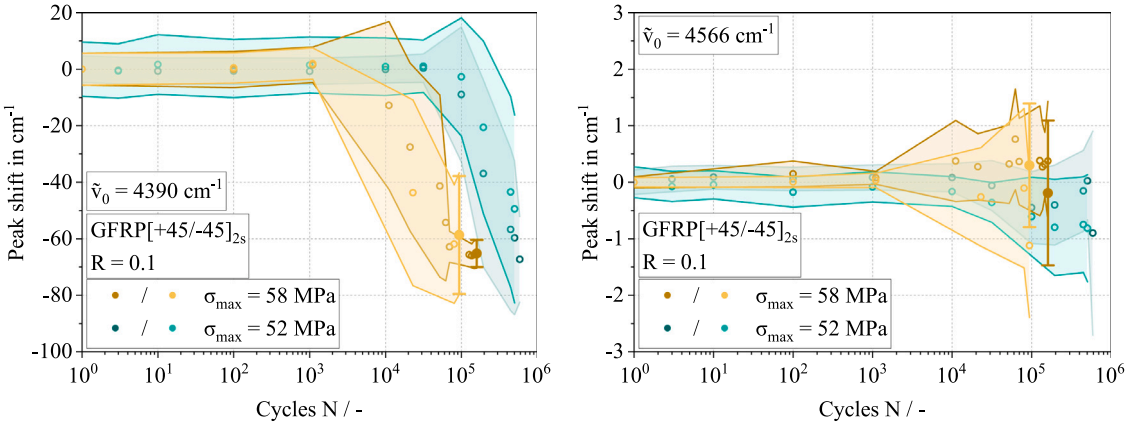

(a) Peak shift of the aromatic combination band at $\tilde{\nu}$ = 4390 cm^{-1} (b) Peak shift of the aromatic combination band at $\tilde{\nu}$ = 4566 cm^{-1}

Fig. 9. Peak shift of two aromatic combination bands over the number of cycles during mechanical fatigue tests.

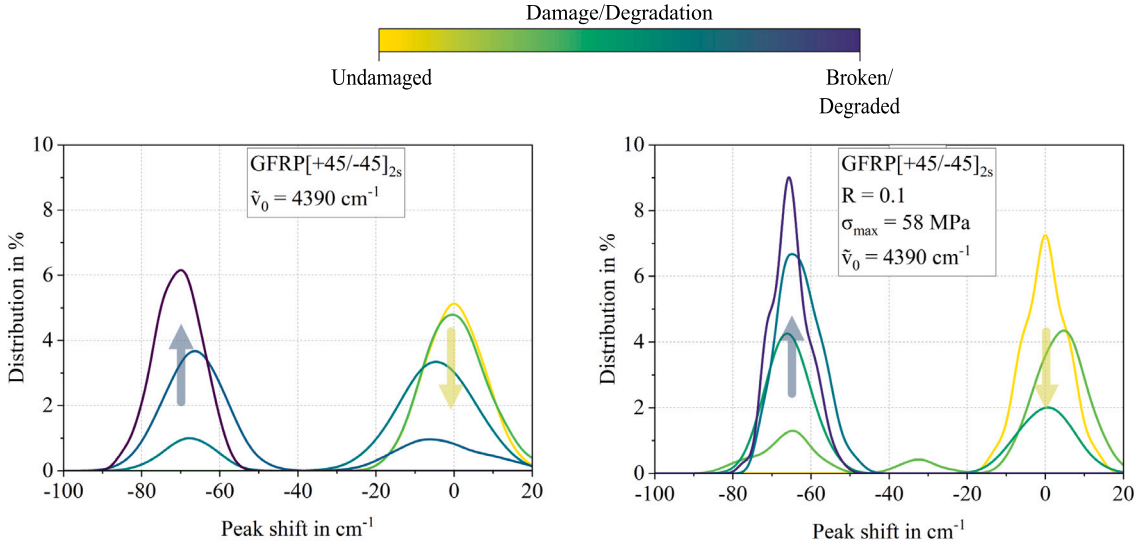

(a) Distribution of the peak shift during stepwise tensile test. (b) Distribution of the peak shift during fatigue tests.

Fig. 10. Distribution of the peak shift of the aromatic combination band at $\nu_0 = 4390$ cm^{-1} for GFRP $[+45/-45]^{2s}$.

scattering of the peak is observed. This behaviour can be explained by residual stresses in the material, resulting from increasing damage accumulation. It is concluded that the increased damage density does not have a significant effect on this wavenumber.

For the second aromatic peak at initially $\tilde{\nu} = 4390\ \mathrm{cm}^{-1}$, no shift in the linear elastic region is observed. However, a significant shift is observed as soon as damage is introduced to the material. The fatigue tests demonstrate a peak shift of approximately equivalent magnitude commencing at 10^3 cycles for the higher load level and shifting approximately a decade to higher cycles for the lower load level, which is comparable to the progression of the stiffness degradation. The persistence of this shift over a period of two months further corroborates that it is not a consequence of tension, as such tension would gradually diminish over time [29]. As demonstrated in Fig. 10, the distributions of the peak shift reveal that this phenomenon is predominantly attributable to the presence of two discernible bands, rather than a shift in band wavenumber. The molecular structure of aromatic ring structures and their symmetry enable the absorption of light at over 20 different wavenumber ranges [20]. In the case of a molecular chain fracture occurring in proximity to these aromatic rings, a potential alteration in their symmetry may ensue, thereby inducing the emergence of this distinct peak. Additionally, it has been observed that the electronegativity of substituent groups can affect the absorption wavenumber of aromatic rings [30]. Thus, a disruption in the molecular chain has the potential to modify the electronegativity of the aromatic ring, consequently altering its absorption wavenumber.

As crack density reaches its maximum under in-plane shear and tensile normal stress aligned with the fibre direction [26], the GFRP $[+45/-45]_{2s}$ layup is expected to exhibit a comparatively strong response in the NIR spectrum. In contrast, other layup configurations are likely to show a significantly weaker effect. It is also noteworthy that, depending on the specimen type, other bands have exhibited peak shifts of varying degrees. However, within a given specimen type, the peak shifts were found to be consistent. For other epoxy materials, this distinct change in wavenumber may not be as clear as it is in these experiments. However, the basic molecular mechanisms will be the same, meaning that these changes can be recognised using stronger mathematical methods, such as multivariate data analysis, even if only a band shoulder is forming.

5. Conclusion

In this study, the practical application of near-infrared (NIR) spectroscopy as a sensitive, non-destructive method of tracking molecular-level responses and mechanical damage in neat epoxy and glass fibre-reinforced plastic (GFRP) composites under stepwise tensile and fatigue loading conditions is demonstrated. Systematically recording NIR spectra throughout mechanical testing provides quantitative evidence of characteristic peak shifts in aromatic absorption bands, which correlate with strain progression and damage accumulation within the materials. The findings underscore the potential of in situ NIR monitoring for real-time assessment of structural damage in fibre-reinforced composites, offering a promising approach for optimising material performance and enhancing the reliability of composite structures in engineering applications.

CRediT authorship contribution statement

Daniel Esse: Writing – review & editing, Writing – original draft, Visualization, Validation, Software, Project administration, Methodology, Investigation, Formal analysis, Data curation, Conceptualization. **Gabriel Sick:** Investigation, Formal analysis. **Frank Henning:** Writing – review & editing, Supervision. **Bodo Fiedler:** Writing – review & editing, Supervision. **Wilfried V. Liebig:** Writing – review & editing, Supervision, Resources, Project administration, Methodology, Investigation, Funding acquisition, Data curation, Conceptualization.

Declaration of competing interest

The authors declare that they have no known competing financial interests or personal relationships that could have appeared to influence the work reported in this paper.

Acknowledgements

This research was funded by the Deutsche Forschungsgemeinschaft (DFG, German Research Foundation), Germany, grant number LI 3675/1-1. The authors acknowledge support by the KIT-Publication Fund of the Karlsruhe Institute of Technology.

Data availability

Data will be made available on request.

References

[1] I.M. Ward, M.A. Wilding, Infrared and Raman spectra of poly (m-methylene terephthalate) polymers, Polymer 18 (4) (1977) 327–335.
[2] K. Holland-Moritz, H.W. Siesler, Infrared spectroscopy of polymers, Appl. Spectrosc. Rev. 11 (1) (1976) 1–55.
[3] J. Mittelhaus, P. Röttger, E. Schill, J. Jacobs, B. Fiedler, Investigation of the ductile deformation potential of microscale epoxy materials, Polym. Test. 128 (2023) 108217.
[4] P. Dirac, Note on the Doppler principle and bohr's frequency condition, in: Mathematical Proceedings of the Cambridge Philosophical Society, vol. 22, Cambridge University Press, 1924, pp. 432–433.
[5] Y. Ozaki, C. Huck, S. Tsuchikawa, S.B. Engelsen, Near-Infrared Spectroscopy: Theory, Spectral Analysis, Instrumentation, and Applications, Springer, 2021.
[6] J. Reynolds, S.S. Sternstein, Effect of pressure on the infrared spectra of some hydrogen-bonded solids, J. Chem. Phys. 41 (1) (1964) 47–50.
[7] M.R. Vanlandingham, R.F. Eduljee, J.W. Gillespie Jr., Moisture diffusion in epoxy systems, J. Appl. Polym. Sci. 71 (5) (1999) 787–798.
[8] V.I. Vettegren', V.B. Kulik, Quantum vibration dynamics and deformation of skeleton of polymer molecules, Polym. Sci. Ser. A 51 (2009) 849–857.
[9] V.I. Vettegren, I.I. Novak, Determination of atomic stress distribution in stressed polymers by infrared spectroscopy, J. Polym. Sci.: Polym. Phys. Ed. 11 (11) (1973) 2135–2142.
[10] L. Salmén, E. Bergström, Cellulose structural arrangement in relation to spectral changes in tensile loading FTIR, Cellulose 16 (2009) 975–982.
[11] R.P. Wool, Mechanisms of frequency shifting in the infrared spectrum of stressed polymer, J. Polym. Sci.: Polym. Phys. Ed. 13 (9) (1975) 1795–1808.
[12] R.M. Badger, A relation between internuclear distances and bond force constants, J. Chem. Phys. 2 (3) (1934) 128–131.
[13] J. Cioslowski, G. Liu, R. Castro, Badger's rule revisited, Chem. Phys. Lett. 331 (5–6) (2000) 497–501.
[14] N. Poisson, G. Lachenal, H. Sautereau, Near-and mid-infrared spectroscopy studies of an epoxy reactive system, Vib. Spectrosc. 12 (2) (1996) 237–247.
[15] B. Degamber, G.F. Fernando, A comparative study on the cure behaviour of thermal-and microwave-processed epoxy resin, J. Near Infrared Spectros 12 (4) (2004) 221–231.
[16] K.E. Chike, M.L. Myrick, R.E. Lyon, S.M. Angel, Raman and near-infrared studies of an apoxy resin, Appl. Spectrosc. 47 (10) (1993) 1631–1635.
[17] V. Strehmel, T. Scherzer, Structural investigation of epoxy amine networks by mid-and near-infrared spectroscopy, Eur. Polym. J. 30 (3) (1994) 361–368.
[18] R. Unger, U. Braun, J. Fankhänel, B. Daum, B. Arash, R. Rolfes, Molecular modelling of epoxy resin crosslinking experimentally validated by near-infrared spectroscopy, Comput. Mater. Sci. 161 (2019) 223–235.
[19] H. Yamasaki, S. Morita, Identification of the epoxy curing mechanism under isothermal conditions by thermal analysis and infrared spectroscopy, J. Mol. Struct. 1069 (2014) 164–170.
[20] J. Workman, L. Weyer, Practical guide and spectral atlas for interpretive near-infrared spectroscopy, Infrared Spectrosc. 2 (2012).
[21] J. Mijović, S. Andjelić, J.M. Kenny, In situ real-time monitoring of epoxy/amine kinetics by remote near infrared spectroscopy, Polym. Adv. Technol. 7 (1) (1996) 1–16.
[22] L. Li, Q. Wu, S. Li, P. Wu, Study of the infrared spectral features of an epoxy curing mechanism, Appl. Spectrosc. 62 (10) (2008) 1129–1136.
[23] B. Min, Z.H. Stachurski, J.H. Hodgkin, G.R. Heath, Quantitative analysis of the cure reaction of DGEBA/DDS epoxy resins without and with thermoplastic polysulfone modifier using near infrared spectroscopy, Polymer 34 (17) (1993) 3620–3627.
[24] C.E. Demers, Fatigue strength degradation of E-glass FRP composites and carbon frp composites, Constr. Build. Mater. 12 (5) (1998) 311–318.

[25] M. Drvoderic, Modeling fatigue damage in composite laminates, Mont. Universität Leoben (2023).
[26] A.W. Wharmby, F. Ellyin, Damage growth in constrained angle-ply laminates under cyclic loading, Compos. Sci. Technol. 62 (9) (2002) 1239–1247.
[27] A.W. Wharmby, F. Ellyin, J.D. Wolodko, Observations on damage development in fibre reinforced polymer laminates under cyclic loading, Int. J. Fatigue 25 (5) (2003) 437–446.
[28] A.V. Movahedi-Rad, T. Keller, A.P. Vassilopoulos, Interrupted tension-tension fatigue behavior of angle-ply gfrp composite laminates, Int. J. Fatigue 113 (2018) 377–388.
[29] M.F. Younes, A. Rahman, Tensile relaxation behaviour for multi layes fiberglass fabric/epoxy composite, Eur. J. Mater. Sci 3 (1) (2016) 1–13.
[30] J.M. Chalmers, Handbook of Vibrational Spectroscopy, John Wiley & Sons, 2001.